Comparison and validation of Airborne Thematic Mapper thermal imagery using ground-based temperature data for Grímsvötn caldera, Vatnajökull, Iceland

S. F. STEWART[1], H. PINKERTON[2], G. A. BLACKBURN[1] & M. T. GUÐMUNDSSON[3]

[1]*Department of Geography, Lancaster University, Lancaster LA1 4YB, UK*

[2]*Department of Environmental Science, Lancaster University, Lancaster LA1 4YB, UK*
(e-mail: s.stewart@Lancaster.ac.uk)

[3]*Institute of Earth Sciences, University of Iceland, Sturlugata 7, IS-101 Reykjavik, Iceland*

Abstract: Grímsvötn, Iceland's most active volcano, is also one of the most powerful geothermal areas in Iceland. This subglacial volcano is located in the centre of Vatnajökull, Europe's largest temperate ice cap, and it erupted most recently in 1998 and 2004. As part of continuing research on heat flux, morphological changes and volcanic processes at Grímsvötn, thermal anomalies were mapped using remote sensing Natural Environmental Research Council (NERC) Airborne Research and Survey Facility (ARSF) data. The 2001 Airborne Thematic Mapper (ATM) thermal images of the Grímsvötn subglacial caldera reveal distinct areas of geothermal activity and provide an overview of the thermal anomalies associated with water and rock exposures. A crater lake located on the 1998 eruption site is shown to have a surface temperature of $30-35\ ^{\circ}$C. There is a good correlation between the ARSF data and ground-based temperature measurements. The thermal images also revealed previously undetected areas of high heat flow. Factors that complicate the interpretation and comparison of different datasets from an ice-covered area include recent cornice collapses and variations in atmospheric humidity. To reduce uncertainty in future missions, temperature measurements should be made at points whose position is well constrained using differential global positioning system. In addition, humidity and temperature measurements should be made at the time of flight.

Subglacial volcanoes are found both beneath cold-based ice sheets in the polar regions and beneath temperate glaciers, such as in Iceland. The type of eruptive activity on a subglacial volcano depends on a number of factors including glacier type, ice thickness and magma chemistry (Guðmundsson *et al.* 1997, 2002; Höskuldsson & Sparks 1997; Bourgeois *et al.* 1998; Einarsson 1999; Smellie 2000, 2002; Tuffen *et al.* 2002; Björnsson 2003). When magma reaches the base of the glacier through a fissure or circular vent underneath glacial ice, it starts to melt the ice. On the surface a depression known as an ice cauldron (Björnsson 1975) is formed as a result of subsidence, with large crevasses forming in a circular pattern in response to ice strain caused by ice melting and the subsequent release of water. Active subglacial volcanic eruptions cannot be studied using traditional field-based methods, because of poor accessibility. Thus, remote sensing (RS) and observations from the air have been the main tools to study such events (Rothery *et al.* 1988; Guðmundsson *et al.* 2004). Moreover, in some cases most of the volcanic edifice may be concealed under hundreds of metres of ice. Many stratovolcanoes with small summit ice caps are often near populated regions, and although not completely subglacial, have similar accessibility problems. However, even remote ice-covered volcanoes are hazardous because of the rapid formation of melt water, which can travel large distances from the volcano. Temperate glaciers are at their pressure melting temperature throughout their thickness, and water can migrate underneath the glacier allowing melt water to flow from the geothermal heat source of an eruption to the edges of the glacier, causing devastating floods known by the Icelandic term, jökulhlaups (Smellie 2000). RS offers a low-risk, global coverage of volcanoes that allows the study of a range of phenomena such as thermal, temporal and topographic variations (Oppenheimer & Rothery 1991). This has the potential to improve our understanding of subvolcanic processes, which are difficult to study using conventional methods, and could lead to better forecasting of eruptions and hazardous events such as jökulhlaups. The objective of this research is to build on present ground-based calorimetric work on thermal anomalies, specifically for inaccessible and hazardous terrain.

Geological setting

The Neovolcanic Zone in Iceland has been subdivided into three rift systems (Fig. 1a), the western, eastern and northern volcanic zones (Einarsson 1999). In southern Iceland, accretion is controlled by NE–SW-trending fissures and faults, whereas mainly north–south-trending lineations are dominant to the north of Vatnajökull. The volcanic fissures of the eastern volcanic zone (EVZ) lie beneath the western side of the Vatnajökull ice sheet (Einarsson *et al.* 1997), Europe's largest temperate ice sheet (Fig. 1b) covering an area of 8300 km^2 in SE Iceland.

Two of the most active volcanic systems in the EVZ are Bárðarbunga and Grímsvötn (Guðmundsson & Björnsson 1991). Both systems are composed of a central volcano and one or two fissure swarms (Saemundsson 1979). Although Bárðarbunga has erupted more magma, Grímsvötn is the more active of the two, with about 60 small eruptions that have deposited tephra over Vatnajökull in the last 800 years (Guðmundsson & Björnsson 1991; Grönvold *et al.* 1995; Larsen *et al.* 1998; Konstantinou *et al.* 2000). Mapping of subglacial topography using radio echo sounding has shown that Grímsvötn is a caldera-type volcano (Björnsson & Einarsson 1990).

Within the Grimsvötn caldera, intense geothermal activity continuously melts the surrounding ice at a rate of 0.2–0.5 km^3 $year^{-1}$ (Björnsson 2003), creating permanent depressions or ice calderas. The meltwater accumulates in the subglacial caldera lake, lifting the water level by 50–100 m over a period of a few years. It is subsequently released in jökulhlaups. When this occurs, the lake level is lowered by 50–100 m in 1–2 weeks, typically releasing 1–2 km^3 of meltwater (Björnsson 2003). Björnsson (1998) described the caldera as being 6–10 km diameter, bordered by the mountain ridge Grímsfjall to the south and subglacial mountains to the north and east (Fig. 1c). The Grímsvötn caldera is divided into three smaller calderas: the main (or south), north and east calderas (Guðmundsson & Milsom 1997). The subglacial lake covers the main caldera and extends into the northern depression at high water levels. The lake covers the areas of highest geothermal activity, and the eruptions in 1922, 1934, 1983, 1998 and 2004 all took place at its southern margin, where geothermal activity is also most intense (Guðmundsson & Björnsson 1991).

The ice-covered Grímsvötn caldera lake has been used as a calorimeter for measuring the heat transfer from magma to ice and melt water, and the rate of accumulation of melt water (Guðmundsson 2003). Studies of geothermal power using calorimetry to convert ice melting rates into heat transfer rates have shown that Grímsvötn is one of the most powerful geothermal areas in the world. The heat output has mostly been in the range of 2000–4000 MW over recent decades (Björnsson & Guðmundsson 1993). However, this work was carried out on the Grímsvötn caldera lake prior to the 1998 eruption, when the lake was believed to be an enclosed system with no leakage. Since the 1998 eruption, increased melting at the ice dam that used to seal Grímsvötn caldera lake has led to leakage from the lake (Guðmundsson 2003). Consequently, calorimetry can no longer be effectively used. Moreover, at the 1998 eruption site, heat has been lost directly to the atmosphere via bodies of open water. Thermal RS has the potential to provide an alternative method of calculating the thermal budget for this volcano. This paper provides the preliminary analysis carried out to extract temperatures and validate the airborne thermal images that will later be used, along with meteorological estimates, to calculate heat flux.

ATM data

The UK Natural Environmental Research Council (NERC) Airborne Remote Sensing Facility's (ARSF) Airborne Thematic Mapper (ATM) sensor is a Daedalus 1268 AZ-16, a passive remote sensor designed to collect radiation reflected and emitted from the Earth's surface from an airborne platform. The scan head optics and detector layout separates the incoming radiation into 11 spectral bands (Table 1) ranging from blue in the visible (VIS) parts of the spectrum to thermal infrared (IR) (Azimuth System 2001). Bands 1–8 cover the VIS and near-IR parts of the spectrum. Bands 9 and 10 are shortwave infrared (SWIR) and band 11 is thermal IR. The thermal band is calibrated in 'real time' using two on-board blackbodies (NERC ARSF 2002), which are imaged by the sensor during each scan before and after the scene pixels (5 m × 5 m) on a scan line. Aerial survey data along three flight lines were collected on 10 and 14 June 2001. The central line was chosen from each flight as these covered the entire Grímsfjall ridge area, an area of 16 km^2. The first stage in processing the ATM data was geometric correction, carried out using AZGCORR software on a UNIX workstation (NERC ARSF 2002). AZGCORR combines the scanned image data with pre- or post-navigation records and then interpolates a map projection, referenced to the output image that has been corrected for aircraft position and altitude (NERC ARSF 2002). The navigation is converted from geographical co-ordinates on global positioning system (GPS) satellite datum, to a suitable survey map projection. The current GPS datum is the WGS84 (World Geodetic System agreed in
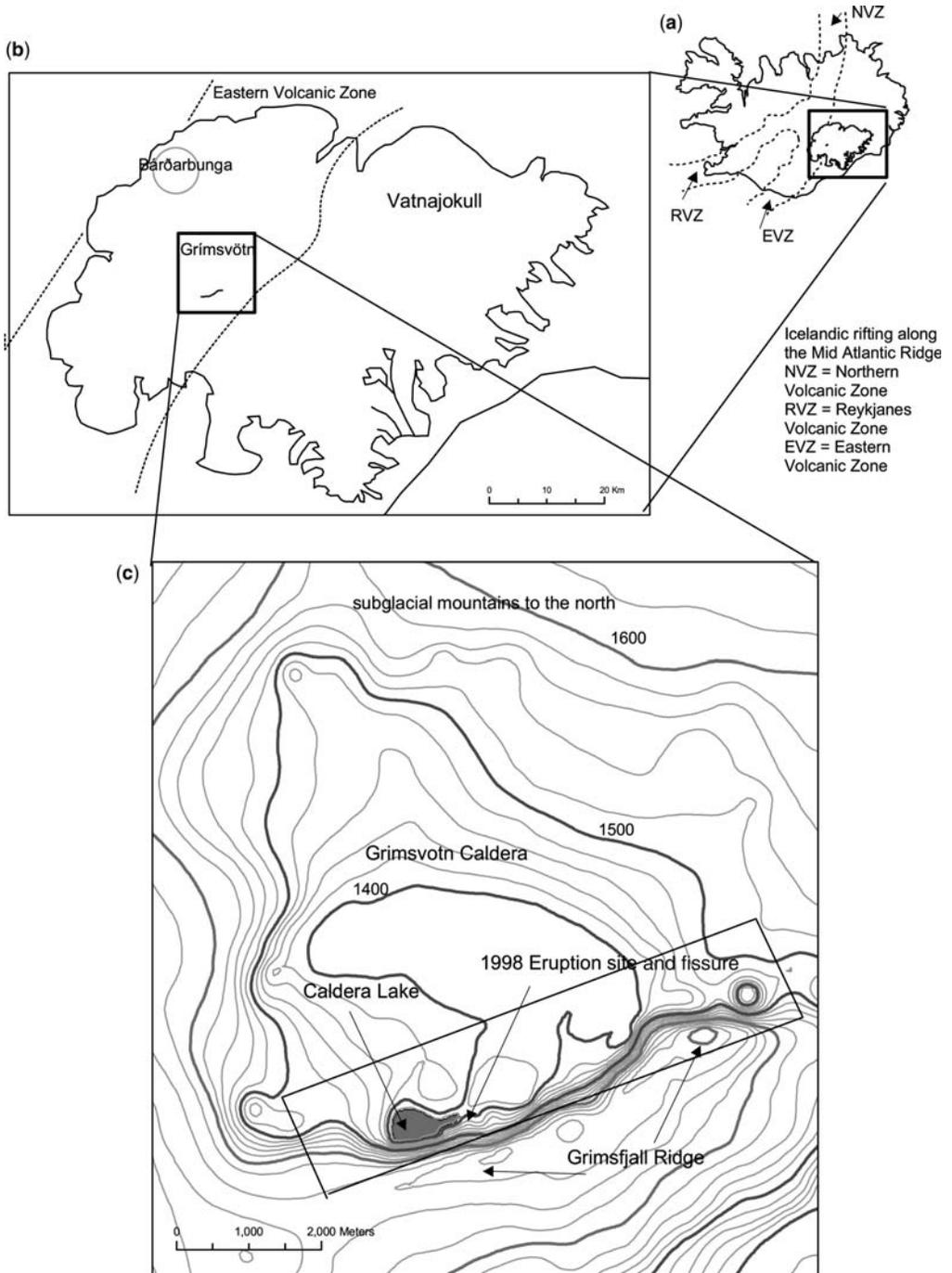
Fig. 1. (**a**) Map of Iceland showing the location of the Vatnajökull ice sheet in relation to the three volcanic zones. (**b**) Map of Vatnajökull showing the location of Grímsvötn caldera together with the 1996 Gjálp fissure and the subglacial volcano, Bárðarbunga. (**c**) Contour map of the Grímsvötn caldera created in 2001 by Icelandic collaborators, using differential GPS, with the Grímsfjall ridge, crater lake, and 1998 eruption site labelled. The rectangular box over the Grímsfjall ridge shows the land area covered by the aerial survey.

Table 1. *Airborne Thematic Mapper (ATM) bands
and relevant parts of the electromagnetic spectrum*

Band	Wavelength (μm)	
1	0.42–0.45	Visible
2	0.45–0.52	
3	0.52–0.60	
4	0.60–0.62	
5	0.63–0.69	
6	0.69–0.75	Near-infrared
7	0.76–0.90	
8	0.91–1.05	
9	1.55–1.75	Shortwave infrared
10	2.08–2.35	
11	8.5–13.0	Thermal infrared

1984). For geocorrection of the ARSF imagery of
Grímsvötn, the WGS 1984 geodetic datum was
chosen, along with UTM zone 28, as this is the
most widely used projection used in this region. A
pixel resolution of 5 m was chosen for each image.

Converting radiance to temperature

The pre-processing carried out by the ARSF con-
verts sensor radiances to surface radiances. In this
conversion, it is assumed that the ground surface
acts as a blackbody. Consequently, an emissivity
of one is used in Planck's law to estimate tempera-
ture. As this is an unrealistic approximation for
most materials, correct temperature data require
the inclusion of more realistic emissivities. The
8–14 μm range includes an atmospheric window
and is the area of peak energy emissions for most sur-
faces at normal Earth surface temperatures (Kahle &
Alley 1992; Lillesand *et al.* 2004). Therefore land
surface materials are often treated as greybodies in
this wavelength range. Close examination of Earth
surface materials shows that emissivity can also
vary with other conditions, such as whether the
material is wet or dry (Liang 2001; Lillesand *et al.*
2004). Early work showed that, to determine accu-
rate temperatures and emissivities, corrected radi-
ance measurements were necessary (Kahle & Alley
1992; Kealy & Hook 1993), and this required atmos-
pheric corrections across the image. No atmospheric
correction was carried out on the images as there was
a lack of atmospheric data collected at the time of the
survey. For the purposes of this research an average
figure for emissivity was used because of the lack of
ground truth observations for land cover type and
atmospheric data.

In the current analysis, a map of emissivity was
derived from land cover based on the visible bands,

where a specific emissivity value was allocated to a
land cover class using a supervised classification
technique (parallelepiped and maximum likelihood
rules) based on 27 training clusters in nine land
cover classes. Figure 2 shows the supervised classi-
fication image used to allocate each emissivity.
Each emissivity is based on published emissivities
(Table 2) taken from Lillesand *et al.* (2004).
Using ENVI (version 3.5), an array was generated
allowing each pixel to be allocated an appropriate
emissivity, dependent on its land cover class.
A second array was produced, to derive a new
blackbody radiance based on radiance emissivity
principles:

$$M_g = M_b \epsilon \qquad (1)$$

where M_g is greybody radiance, M_b is blackbody
radiance and ϵ is emissivity.

According to Planck's law, the temperature is
equivalent to the area beneath a spectral radiance
curve. Using the program of A. K. Wilson (pers.
comm.) the spectral radiance curve was separated
into 141 wavelength divisions based on the sensor
response. These wavelength divisions are then
used as the wavelengths for temperature conver-
sion. Using Planck's law, a temperature of 273 K
is assumed initially, from which the program
calculates a radiance for the given wavelength
band, sensor response and temperature. Equation
(2) is a variation of Planck's formula, with the
added sensor response from the program of
A. K. Wilson (pers. comm.):

$$M_\lambda = \frac{C_1 \lambda^{-5} \, \text{resp}}{\exp(C_2/\lambda T) - 1} \qquad (2)$$

where M_λ is the radiant exitance, the total energy
radiated in all directions by a unit area in a unit time
(Curran 1992); spectral radiance constants $C_1 =$
119095879.96 Wm^2 and $C_2 = 14387.75225$ Wm^2;
resp. is the ATM sensor response, divided into 141
wavelengths; λ is the wavelength (μm); T is tempera-
ture in Kelvin. The program continues for every pixel
in the image until all pixels have a temperature
assigned within a new array.

The images were exported from ENVI as Geo-
Tiffs, for subsequent analysis in ERDAS Imagine
and ArcGIS. The images were imported into
ArcMap where, to aid further interpretation, they
were classified into 14 temperature bands, each
with a specific colour attributed to a 5 °C range.
Figure 3 shows a colour composite ATM image,
overlain by a temperature image with colour
palette of 5 °C intervals. All temperatures below
0 °C are shown as colourless, to reflect the snow
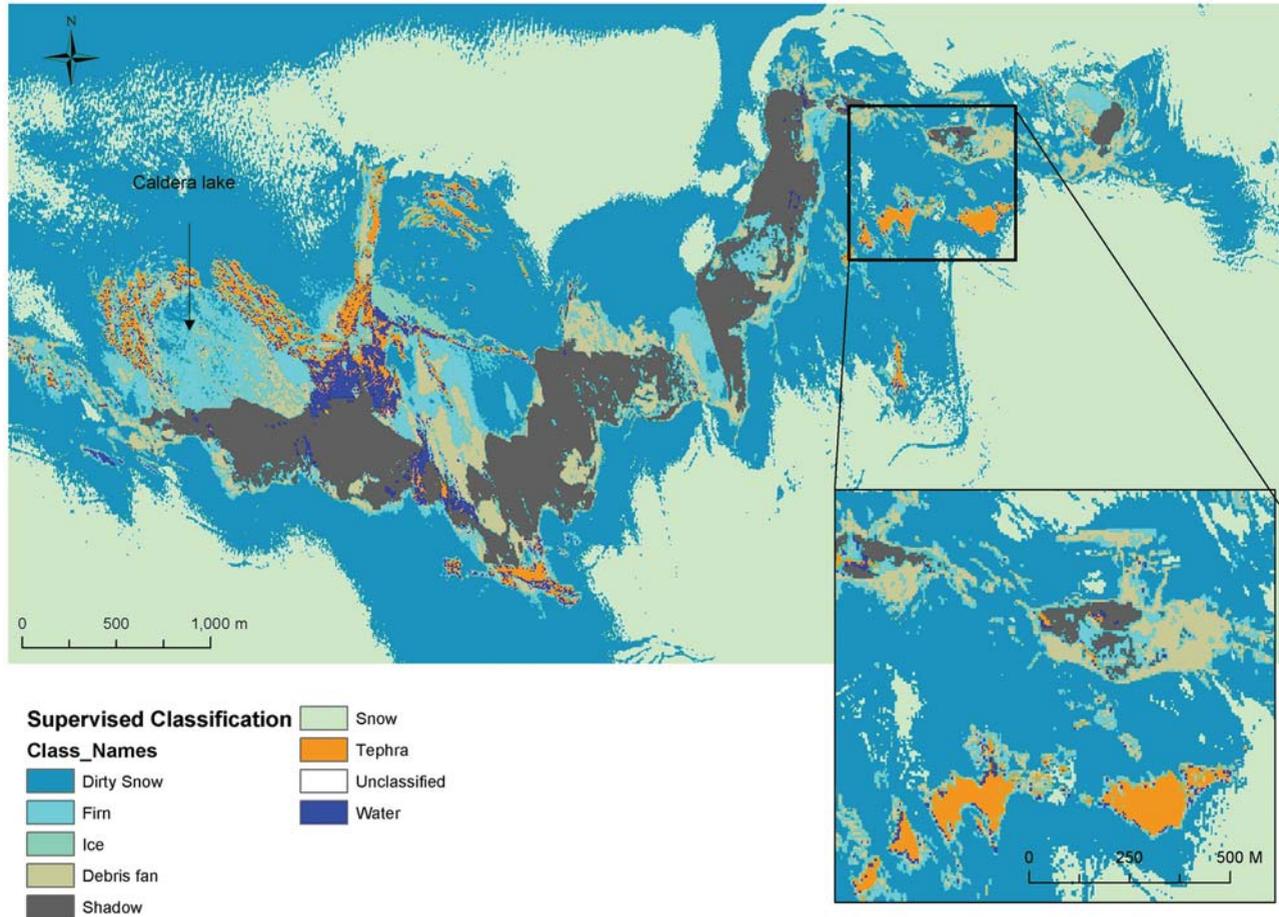and ice cover. The higher-temperature areas are

Fig. 2. Supervised classification image using 27 training classes over nine land cover types, including firn (intermediate class between snow and ice) and screefan (a combination of scree slopes and debris fan deposits). The inset shows an example of the increased pixel detail along the Grímsfjall ridge.

Table 2. *Emissivity values allocated to land cover classes (Lillesand* et al. *2004)*

Land cover class	Emissivity
Ice	0.975
Dirty snow	0.975
Basalt	0.96
Firn	0.975
Water	0.985
Screefan	0.96
Tephra	0.96
Snow	0.98
Shadow	1

either in the crater lakes, or are areas of rock or ice covered by tephra, such as the 1998 eruption site, shown in the inset of Figure 3. The dark area is the topographic shadow of the Grímsfjall ridge for which no thermal data can be collected.

Thermal analysis

Ground-based temperature data collected from unconsolidated tephra within the 1998 eruption crater on 4 June 2001 by Icelandic collaborators were overlain on the thermal images. The co-ordinates of the sample points were collected using a Trimble Pathfinder differential global positioning system (DGPS) instrument with an accuracy of 1–2 m. The point source temperatures were collected from the top 10 cm of tephra, using an Ebro platinum thermometer probe, with a precision of 0.1 °C and accuracy of 0.3 °C, along seven NW–SE lines, with approximately three points on each line, depending on accessibility. Unfortunately, only a small number of temperature measurements were collected, because of the hazardous terrain.

An attempt was made to compare the airborne and ground-based temperature data by identifying specific pixels (5 m × 5 m in size) within which each of the ground sample points were located. However, this revealed that the geometric correction of the ATM imagery was insufficiently accurate to allow this point within specific pixel comparison. The inadequate geometric correction of the imagery was attributable to the inability to incorporate a digital elevation map (DEM) of adequate spatial resolution into the geocorrection procedure. This problem could not be resolved using ground control points to perform further geocorrection of the imagery, as no ground survey points could be found that were also identifiable in the imagery. A further difficulty in comparing airborne and ground targets was that each ground measurement recorded the temperature of the small local area in contact with the thermometer, whereas the

temperature recorded in the ATM data was an integrated value derived from a 5 m × 5 m area of ground. Within each 5 m × 5 m area considerable variability in surface temperatures may exist, as a result of spatial variations in surface properties, in which case a single point temperature measurement is unlikely to be representative of the area as a whole. Figure 3 shows how variable the temperatures across a specific area of the ground can be, especially in areas of high geothermal activity, where there are numerous fumaroles and steam vents. In an attempt to overcome this problem and the difficulties associated with geocorrection of the ATM imagery, the following method was adopted for comparing ground and airborne temperature data.

An image composed of pixels of the same size as the ARSF data (5 m × 5 m), was constructed by interpolating the ground-based point temperature data. A number of interpolation techniques are currently used in geographical information systems (GISs) (Oliver & Webster 1990). Some of the more statistically simple systems lose detail because of smoothing (Oliver & Webster 1990). Kriging is a technique based on the statistical approach of regionalized variable theory (Mather 1999). It was selected because it allows for optimization of unbiased results along with an indication of the confidence limits in the analysis of individual datasets shown by a variogram created during this type of analysis. A variogram is a measure of the variance between data as a function of distance (Mather 1999). The ordinary linear kriging method available within ArcMap was used, with the z field being temperature, a search radius of 10 and output cell size of 5 m, to produce a pixelated rectangular grid.

The kriging method assumes that each pixel measurement is representative of a specific point within that pixel. However, for most measurements this will be invalid. The ATM image in Figure 3 shows that adjacent pixels can have a temperature difference of up to 25 °C. Consequently, temperature variations greater than 25 °C may not be unusual within 1 pixel. There is also a natural tendency, when making measurements in the field, to be drawn to the highest temperatures even when attempting random sampling. There is less confidence in regions away from the sampling sites, as those areas may have the highest variance. Hence a linear 200 m profile diagonally through the temperature points was chosen (i.e. the area within which we can have most confidence in the interpolation results as indicated by minimal variance). Figure 4 shows the interpolated temperature points and the location of the profile. Blocks of 3 pixels astride the profile line were averaged to produce the temperature value for each location
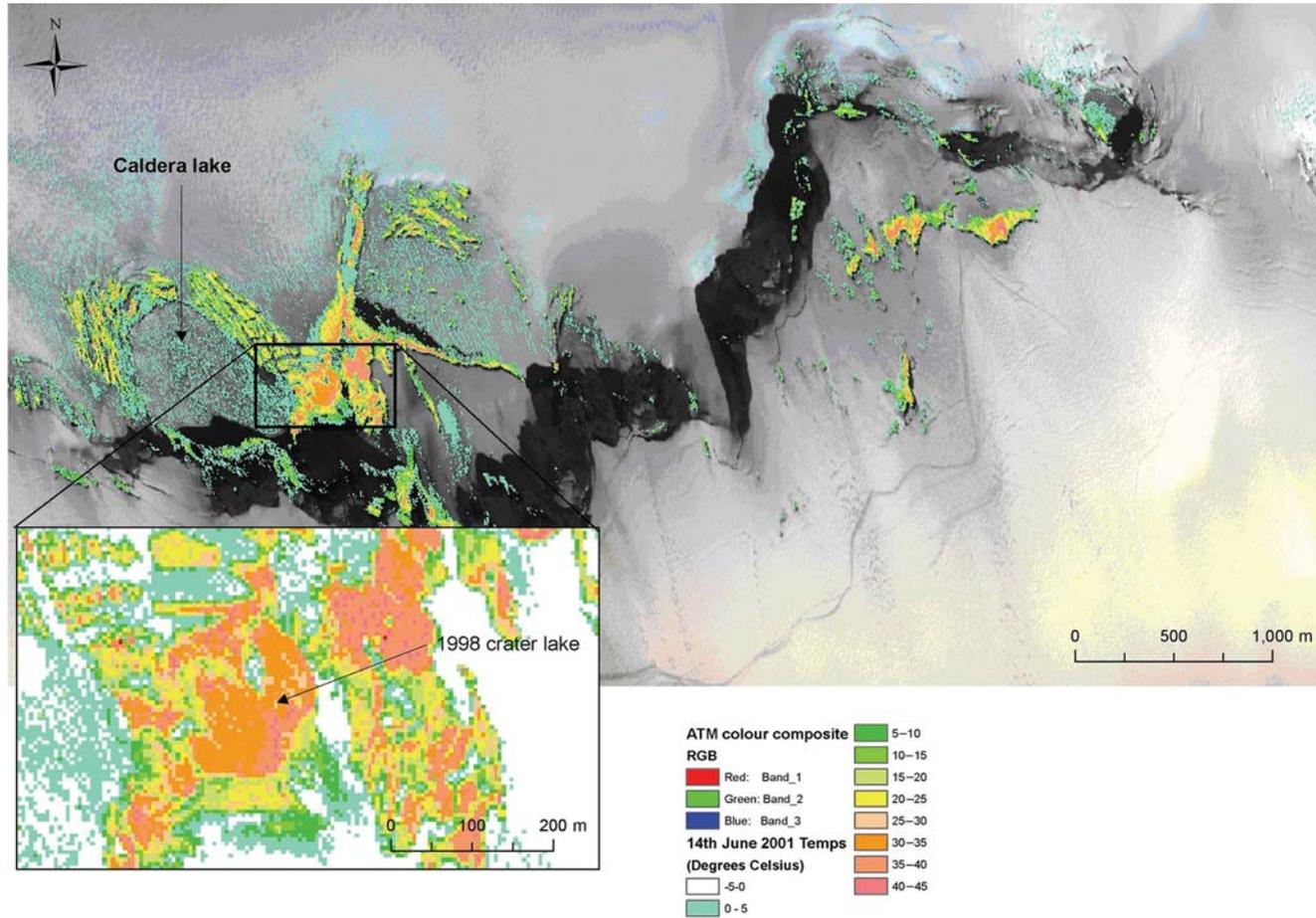
Fig. 3. A temperature image, overlying a colour composite ATM image (Bands 1, 2 and 3 in red, green and blue, respectively). All the temperatures above 0 °C are colour coded in 5 °C intervals. The enlarged area is the 1998 eruption site.
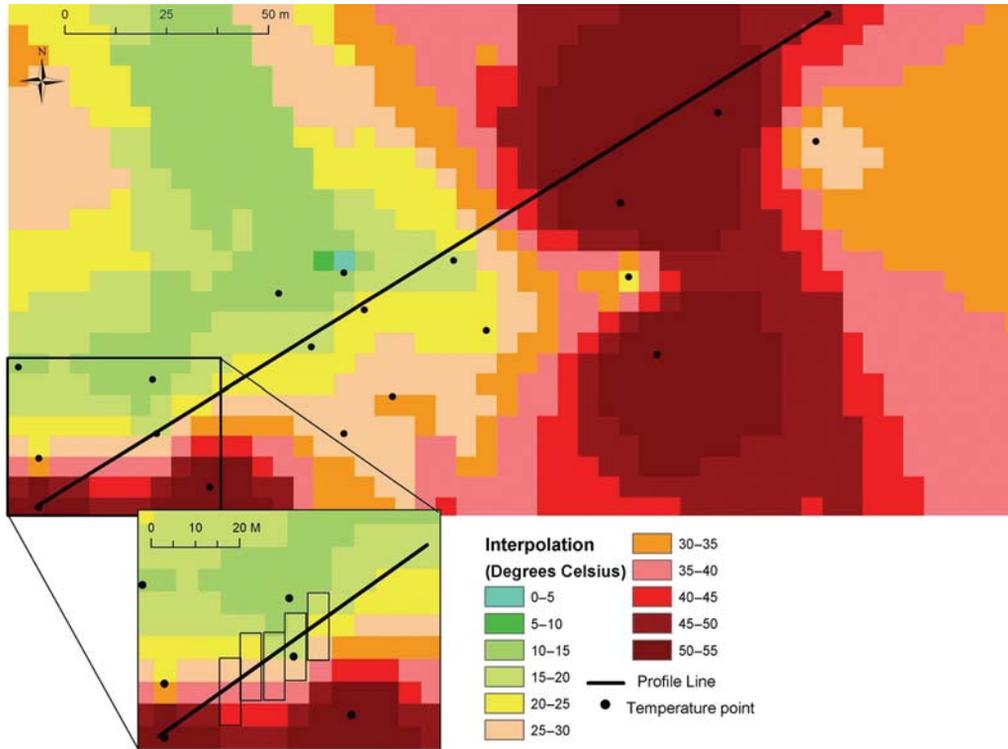
Fig. 4. Interpolation of ground-based temperature points displayed as 5 m pixels using the RGB palette in 5 °C
intervals. The locations of the temperature points and line of profile are shown. In the inset, boxes of 3 pixels length
show how the average temperatures were taken along the profile.

along the profile (Fig. 4 inset). In this way errors
associated with the registration of the temperature
points with the thermal image and errors associated
with uncertainty within pixels were minimized.
Figure 5 shows the 1998 eruption site, the location
of the 2001 ground-based temperature points, and
the overlaid interpolation. Comparison of the two
images using the coloured pixels shows that the
two approaches, in some cases, produce similar
temperatures. The difference in colour depicted in
the two images is explained by the fact that the
ground-based images have overall higher tempera-
tures because of the high-temperature sampling
points.

Figure 6a shows a comparison between the
ground-based and remote sensing temperatures.
The graph shows that, along the central part of the
profile from 40 to 120 m, the temperatures are
similar, with the ATM profiles showing slightly
elevated temperatures compared with the ground-
based ones. The temperatures correlate reasonably
well, considering the two datasets were acquired
almost a week apart. The maximum variation is of

10 °C. The high correlation is supported by the
visual spatial pattern in Figure 5. However, there
are anomalous high-temperature areas in the first
20 m and the last 80 m of the ground-based temp-
erature profile compared with the ATM data.
Within the first 20 m of the profile, there are a
number of anomalous points (Fig. 6a) that have
good coverage by ground measurements. The
thermal images show lower temperatures than the
ground-based interpolation. This could be
explained by pixel-integrated temperatures within
the imagery that appear to lower the overall temp-
erature, especially in the last 80 m of the profile,
where ground temperatures are substantially
higher than the aerial image temperatures. An
alternative explanation for this could be related to
the low atmospheric pressure measured at the
Grímsvötn meteorological station at 160 m above
sea level (m a.s.l.), as this can cause an increase
in steam emissions along the Grímsfjall ridge. The
air pressure was measured as 808 hPa on 4 June at
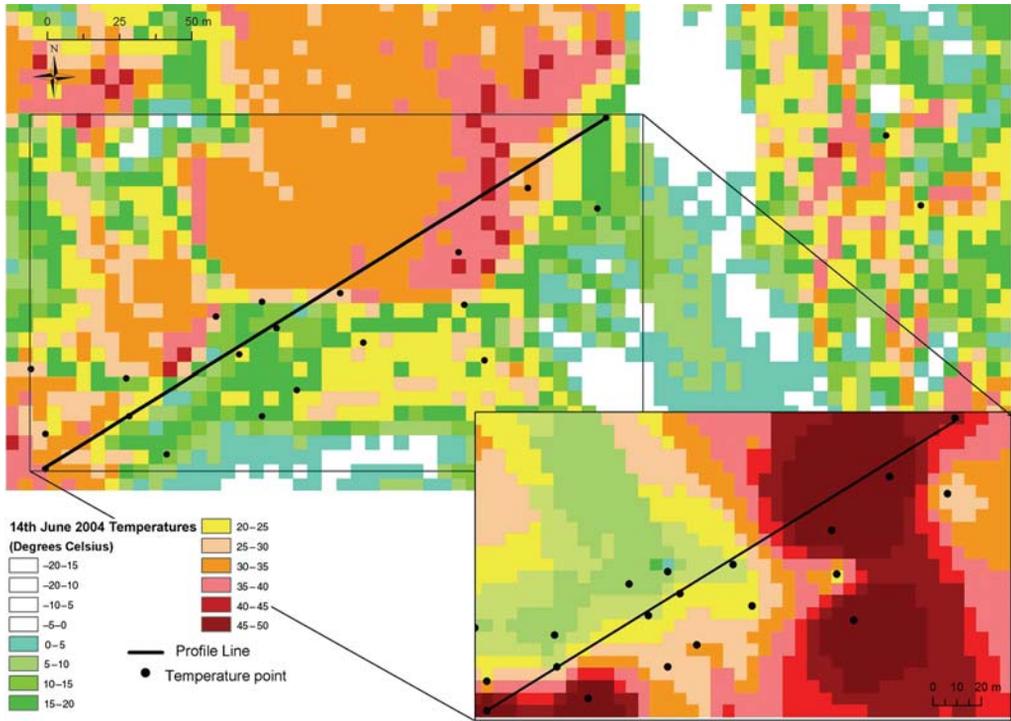the time of the ground survey, as opposed to
823 hPa on 10 June 2001.

Fig. 5. Locations of the temperature points collected on 4 June 2001 within the 1998 eruption crater, shown on a temperature image for 14 June 2001, together with the profile line used for the analysis. The smaller inset shows the interpolated 2001 temperatures using the same colour scheme.

Figure 8b is a graph comparing the temperatures of the two ATM images (10 and 14 June 2001). Overall the temperatures are in agreement, except in the first 50 m of the profile. An explanation for the difference between the ATM temperatures as well as the ground-based temperatures could be related to differences in the conditions in which the images were collected; that is, the height difference of aircraft (214 m); the look angle because of the position of the flight line (the ATM sensor was almost directly above the lake on 14 June (at an angle of 6.46°), but was at an angle of 37.87° from normal on 10 June 2001; time of day (10:00 h on 14 June and 16:00 h on 10 June) causing changes in the angle of the Sun and solar reflectance; rather than a change in the ground conditions. Atmospheric attenuation is a major contributor to these differences, as the two surveys were flown from different altitudes. Although no atmospheric correction was made on the images, an atmospheric attenuation model derived from a FLIR Systems ThermoCAM was used to make an atmospheric transmission correction following analysis. For a relative humidity range of 30–70%, a maximum error of up to 17 °C is possible

for an altitude of 1469.03 m (for 10 June 2001), and 15.3 °C at an altitude of 924.37 m (for 14 June 2001). However, based on this information the error could be as much as 17 °C if there was an extreme change in humidity over the 4 days between flights. Additional errors will arise as a consequence of instrument drift, geometric correction, and the co-registration of temperature points to the ATM images. Figure 7 shows the error applied to the 200 m profile shown in Figure 6a and b. Given the size of the error bars, the temperatures are very similar, save for a few high ground-based temperatures at the beginning and end of the profile.

Comparisons of ground-based temperature data with ATM temperature imagery reveal similarities in results. However, there are problems combining the different techniques, as it is difficult to compare temperatures at specific locations and times because of pixel integrated temperatures and topographic variations. It is possible to derive spatial variations and change over time, but there ideally needs to be a longer time frame between the acquisitions of temperature imagery. However, there is still a need for additional ground observations, including
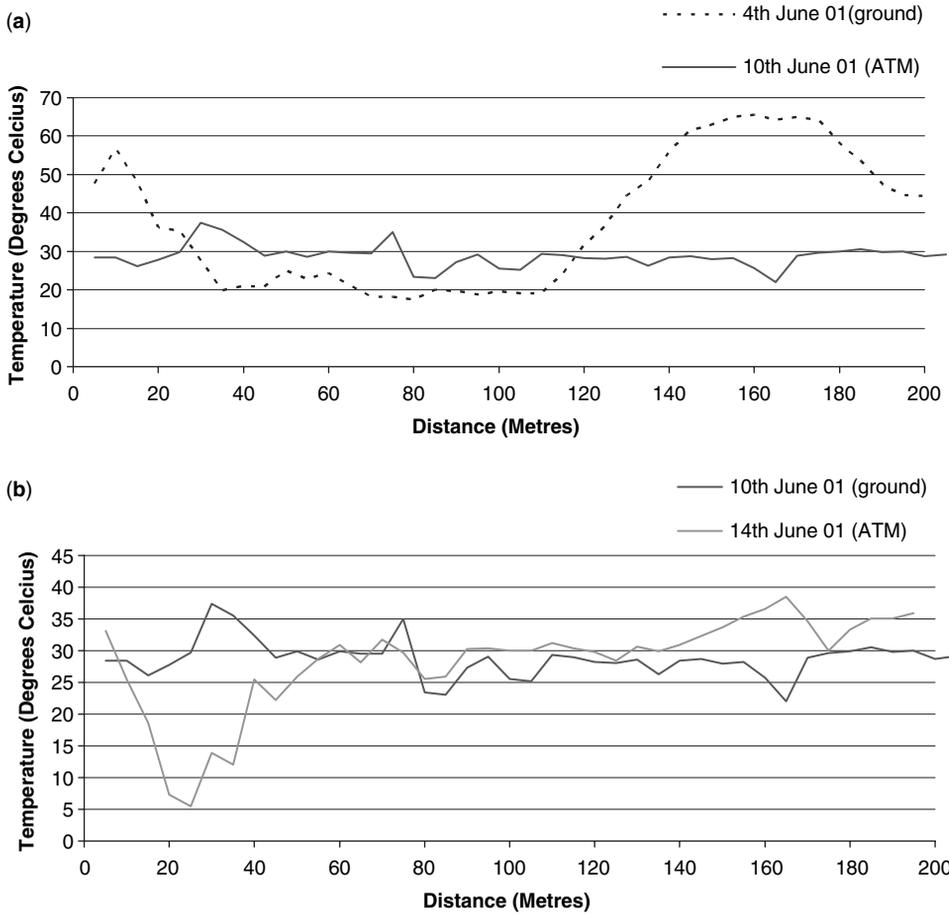
(a)

(b)

Fig. 6. (**a**) The 200 m long least variance temperature profiles, within the 1998 eruption crater, comparing the ground-based (4 June 2001) and airborne (10 June 2001) temperature data. (**b**) Comparison of ATM temperature profiles for 10 and 14 June 2001.
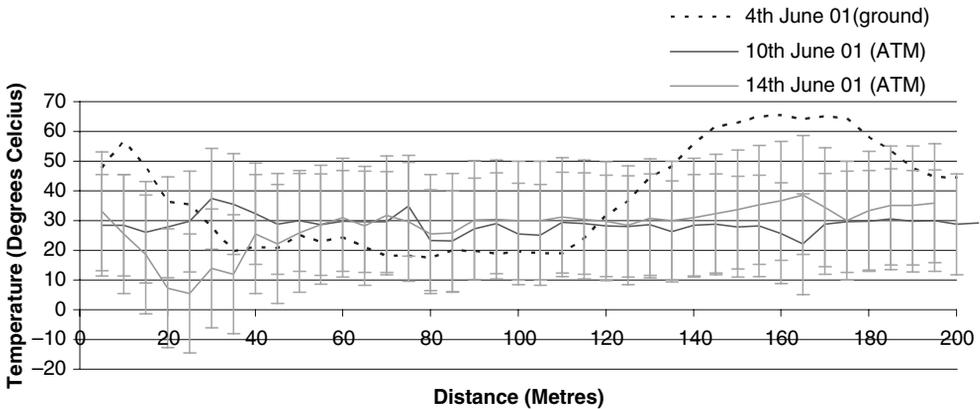

Fig. 7. Graph to show the maximum error (of 17 °C) that could be caused by atmospheric attenuation, along the 200 m profile.
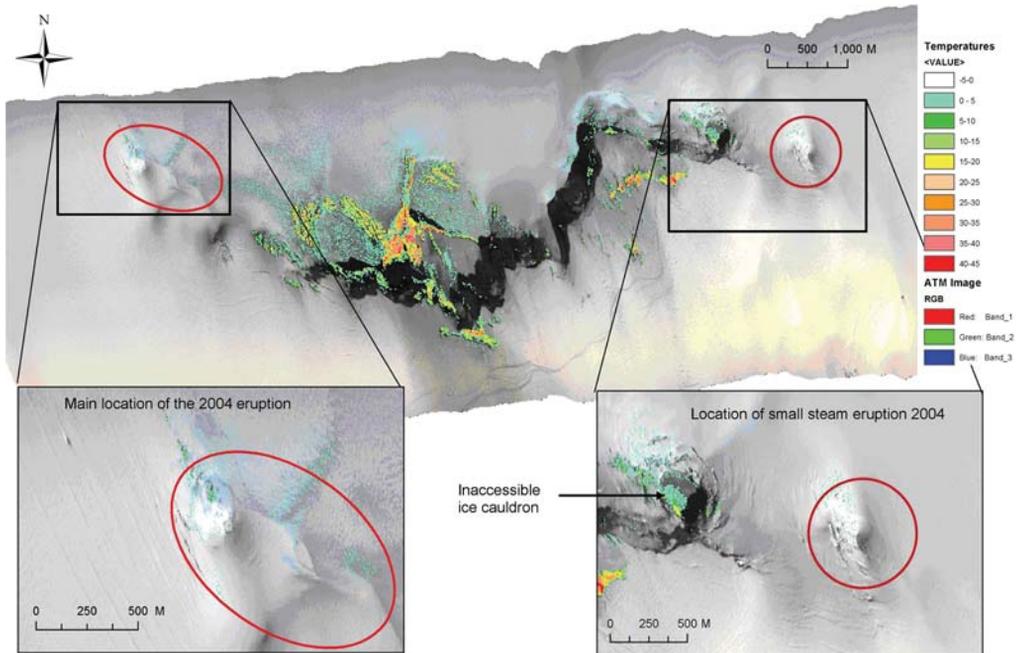
Fig. 8. A temperature image, overlying a colour composite ATM image (Bands 1, 2 and 3 in red, green and blue, respectively). All the temperatures above 0 °C are colour-coded in 5 °C intervals. Also shown are the main locations where the 2004 eruption broke through the ice (red circles).

meteorological and atmospheric measurements, and a larger number of temperatures.

Evaluating usefulness

A primary project aim was to compare 'modelled' temperature data from the ARSF images with ground truthing measurements and to use the ARSF imagery to observe and map thermal anomalies at Grímsvötn. Once the analysis is complete, it is hoped that the data will lead to an analysis of heat flux, as this will lead to improved understanding of the processes at work within such a dynamic region.

The NERC ARSF visible and thermal IR images reveal the presence of a number of ice cauldrons around the Grímsvötn caldera and in areas that cannot be measured in the field. This includes inaccessible parts of the Grímsfjall ridge, such as the small water-filled ice cauldron on the left-hand side on the eastern inset (Fig. 8). As the ice cauldron has steep-sided ice walls there is no way, other than by using RS, to obtain water temperature data. From the thermal images pixel integrated temperatures range from −0.96 to 25.09 °C on both days. A high-temperature trend along the southern section of both the ice cauldron lake and the 1998 crater lake,

following the trend of the 1998 eruption fissure, is visible. When compared with ground-based photographs there is steam visible across these sections of the lakes.

Guðmundsson (2003) showed the role of heat transfer from magma to ice and melt water using calorimetry. Precursory evidence of an eruption would be in the melt water rather than on the rock or ice surface. Therefore temperatures recorded from the crater lake or ice cauldrons are fundamental to monitoring Grímsvötn. Figure 9 is a frequency distribution curve of the 1998 eruption site crater lake temperatures from the two thermal images. This shows that the overall distribution of temperatures is similar for the two flights. As noted above, the sensor was almost directly above the lake on 14 June (at an angle of 6.46°), but was at an angle of 37.87° from normal on 10 June. The oblique nature of the view affects the area imaged. The lake water data show that there is similarity between the two flight days. However, there are still discrepancies shown within the ground-based profile data. Atmospheric attenuation is a major contributor to these differences, as the two surveys were flown from different altitudes (i.e. 1469.03 m a.s.l. and 924.37 m a.s.l., respectively). Additional errors will arise as a consequence of instrument drift and related to geometric correction.
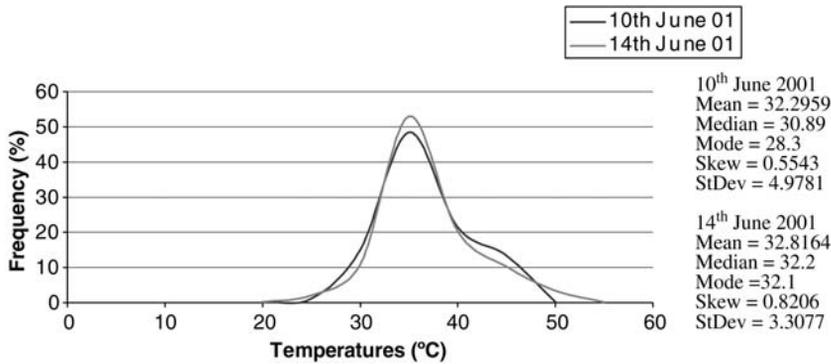
Fig. 9. Frequency distribution curve of the 1998 eruption site crater lake temperatures from the two thermal images. This shows that the overall distribution of temperatures is similar for the two flights. Percentage frequency was used to standardize the histograms.

Following the November 2004 eruption, it has been possible to assess whether the 2001 imagery contains any information that could be useful in the identification of the 2004 eruption site. Figure 8 shows the thermal image overlying the ATM colour composite image, with the locations of the main and smaller steam eruptions marked. The main eruption site (red oval) in the southwestern corner of the cauldera shows the presence of an ice cauldron but no thermal anomaly. The same is true for the smaller steam eruption (red circle) in the southeastern corner. This is not unexpected, as the 2004 eruption was accompanied by the rapid opening of a fissure system, possibly as a consequence of dyke injections; thus it is unlikely that a precursory thermal region would be detectable 3 years before the 2004 eruption.

Conclusion

Thermal imagery collected using instruments deployed on the NERC ARSF aircraft in June 2001 can be used to give an estimate of temperature distribution along the Grímsfjall ridge. The thermal images give an overall view of thermal anomalies along the area of rock and water exposures at Grímsvötn and reveal elevated temperature regions that were not detected during ground-based measurements. These images allow inaccessible areas to be monitored. As two thermal images collected 4 days apart have shown, there are sometimes large apparent temperature differences on this time scale. The reasons for these are varied, including atmospheric attenuation and image acquisition differences. This will have to be taken into account during any future surveys, along with the need to ensure adequate ground control, good on-board GPS, day and night imagery, and

measurement of humidity and atmospheric conditions at the time of the flight. This would allow an appropriate atmospheric correction to be included as part of the data processing, and this would reduce uncertainties within the data. In conclusion, in spite of the errors, the ground-based and ARSF temperatures are in reasonable agreement where ground control temperatures were measured, allowing us to have confidence in the temperatures collected from this volcano. The temperature data collected during the 2001 survey will be used to constrain the total heat budget from Grímsvötn, using meteorological data to estimate heat flux from areas of open water.

References

AZIMUTH SYSTEM 2001. AZ-16 airborne remote sensing control display and data acquisition system. *AZGCORR User Guide 2001*. Nerc, Swindon.

BJÖRNSSON, H. 1975. Subglacial water reservoirs, jökulhlaups and volcanic eruptions. *Jökull*, **25**, 1–15.

BJÖRNSSON, H. 1998. Hydrological characteristics of the drainage system beneath a surging glacier. *Nature*, **395**(6704), 771–774.

BJÖRNSSON, H. 2003. Subglacial lakes and jökulhlaups in Iceland. *Global and Planetary Change*, **35**, 255–271.

BJÖRNSSON, H. & EINARSSON, P. 1990. Volcanoes beneath Vatnajökull, Iceland: evidence from radio echo-sounding, earthquakes and jökulhlaups. *Jökull*, **40**, 147–168.

BJÖRNSSON, H. & GUÐMUNDSSON, M. T. 1993.
Variations in the thermal output of the subglacial
Grímsvötn Caldera, Iceland. *Geophysical Research
Letters*, **20**, 2127–2130.

BOURGEOIS, O., DAUTEUIL, O. & VAN VLEIT-LANÖE, B.
1998. Pleistocene subglacial volcanism in Iceland:
tectonic implications. *Earth and Planetary Science
Letters*, **164**, 165–178.

CURRAN, P. J. 1992. *Principles of Remote Sensing*.
Longman Scientific and Technical, Harlow, England.

EINARSSON, P. 1999. *Geology of Iceland: Rocks and
Landscape*. Mál og Menning, Reykjavik, Iceland.

EINARSSON, P., BRANDSDÓTTIR, B., GUÐMUNDSSON,
M. T., BJÖRNSSON, H., GRÖNVOLD, K. &
SIGMUNDSSON, F. 1997. Centre for the Icelandic
hotspot experiences volcanic unrest. *EOS Trans-
actions, American Geophysical Union*, **78**(35), 369
and 374–375.

GRÖNVOLD, K., OSKARSSON, N., JOHNSEN, S.,
CLAUSEN, H., HAMMER, C. U., BOND, G. & BARD,
E. 1995. Ash layers from Iceland in the Greenland
GRIP ice core correlated with oceanic and land sedi-
ments. *Earth and Planetary Science Letters*, **135**,
149–155.

GUÐMUNDSSON, M. T. 2003. Melting of ice by magma–
ice–water interactions during subglacial eruptions as
an indicator of heat transfer in subaqueous eruptions.
In: ÍWHITE, J. D. L., SMELLIE, J. L. & CLAGUE, D.
(eds) *Explosive Subaqueous Volcanism*, Geophysical
Monograph, American Geophysical Union, **140**,
61–72.

GUÐMUNDSSON, M. T. & BJÖRNSSON, H. 1991. Erup-
tions in Grímsvötn 1934–1991. *Jökull*, **41**, 21–46.

GUÐMUNDSSON, M. T. & MILSOM, J. 1997. Gravity
and magnetic studies of the subglacial Grímsvötn
volcano, Iceland. Implications for crustal and
thermal structure. *Journal of Geophysical Research*,
102, 7691–7704.

GUÐMUNDSSON, M. T., SIGMUNDSSON, F. &
BJÖRNSSON, H. 1997. Ice–volcano interaction of
the 1996 Gjálp subglacial eruption, Vatnajökull,
Iceland. *Nature*, **389**, 954–957.

GUÐMUNDSSON, M. T., PÁLSSON, F., BJÖRNSSON, H. &
HÖGNADÓTTIR, TH. 2002. The hyaloclastite ridge
formed in the subglacial 1996 eruption in Gjálp,
Vatnajökull, Iceland: present-day shape and future
preservation. *In*: SMELLIE, J. L. & CHAPMAN, M. G.
(eds) *Volcano–Ice Interaction on Earth and Mars*.
Geological Society, London, Special Publications,
202, 319–335.

GUÐMUNDSSON, M. T., SIGMUNDSSON, F., BJÖRNS-
SON, H. & HÖGNADÓTTIR, TH. 2004. The 1996 erup-
tion at Gjálp, Vatnajökull ice cap, Iceland: efficiency
of heat transfer, ice deformation and subglacial water
pressure. *Bulletin of Volcanology*, **66**, 46–65.

HÖSKULDSSON, A. & SPARKS, R. S. J. 1997.
Thermodynamics and fluid dynamics of effusive
subglacial eruptions. *Bulletin of Volcanology*, **59**,
219–230.

KAHLE, A. B. & ALLEY, R. E. 1992. Separation of temp-
erature and emittance in remotely sensed radiance
measurements. *Remote Sensing of Environment*, **42**,
107–111.

KEALY, P. S. & HOOK, S. J. 1993. Separating temperature
and emissivity in thermal infared multispectral scanner
data: Implications for recovering land surface temp-
eratures. *IEEE Transactions on Geoscience and
Remote Sensing*, **13**, 1155–1164.

KONSTANTINOU, K. I., NOLET, G., MORGAN, W. J.,
ALLEN, R. M. & PRITCHARD, M. J. 2000. Seismic
phenomena associated with the 1996 Vatnajökull erup-
tion, central Iceland. *Journal of Volcanology and
Geothermal Research*, **102**, 169–187.

LARSEN, G., GUÐMUNDSSON, M. T. & BJÖRNSSON, H.
1998. Eight centuries of periodic volcanism at the
center of the Iceland hot spot revealed by glacier
tephrastratigraphy. *Geology*, **26**, 943–946.

LIANG, S. 2001. An optimisation algorithm for separating
land surface temperature and emissivity from multi-
spectral thermal infrared imagery. *IEEE Transactions
on Geoscience and Remote Sensing*, **39**(2), 264–274.

LILLESAND, T. M., KIEFER, R. W. & CHIPMAN, J. W.
2004. *Remote Sensing and Image Interpretation*, 5th
edn. Wiley, New York.

MATHER, P. M. 1999. *Computer Processing of Remotely
Sensed Images. An Introduction*, 2nd edn. Wiley,
Chichester.

NERC ARSF 2002. *User Manual. Airborne Thematic
Mapper (ATM) and Integrated Data System (IDS).
Version 2*, Nerc, Swindon.

OLIVER, M. A. & WEBSTER, R. 1990. Kriging: a method
of interpolation for geographical information systems.
*International Journal of Geographical Information
Systems*, **4**(3), 313–332.

OPPENHEIMER, C. & ROTHERY, D. A. 1991. Infrared
monitoring of volcanoes by satellite. *Journal of the
Geological Society, London*, **148**, 563–569.

ROTHERY, D. A., FRANCIS, P. W. & WOOD, C. A. 1988.
Volcano monitoring using short wavelength infrared
data from satellites. *Journal of Geophysical Research*,
93(B7), 7993–8008.

SAEMUNDSSON, K. 1979. Outline of the geology of
Iceland. *Jökull*, **29**, 7–28.

SMELLIE, J. L. 2000. Subglacial eruptions. *In:*
SIGURDSSON, H. (ed.) *Encyclopaedia of Volcanoes*.
Academic Press, New York, 403–418.

SMELLIE, J. L. 2002. The 1969 subglacial eruption on
Deception Island (Antarctica): events and processes
during an eruption beneath a thin glacier and impli-
cations for volcanic hazards. *In*: SMELLIE, J. L. &
CHAPMAN, M. G. (eds). *Volcano–Ice Interaction on
Earth and Mars*. Geological Society, London,
Special Publications, **202**, 59–79.

TUFFEN, H., PINKERTON, H., McGARVIE, D. W. &
GILBERT, J. S. 2002. Melting of the glacier base
during a small-volume subglacial rhyolite eruption:
evidence from Bláhnúkur, Iceland. *Sedimentary
Geology*, **149**, 183–198.